Geomechanics and Engineering, *Vol. 7, No. 4 (2014) 431-458*
DOI: http://dx.doi.org/10.12989/gae.2014.7.4.431

Multivariate adaptive regression splines model for reliability assessment of serviceability limit state of twin caverns

Wengang Zhang [a] and Anthony T.C. Goh [*]

School of Civil and Environmental Engineering, Nanyang Technological University, 639798 Singapore

(*Received October 10, 2013, Revised March 19, 2014, Accepted July 02, 2014*)

Abstract. Construction of a new cavern close to an existing cavern will result in a modification of the state of stresses in a zone around the existing cavern as interaction between the twin caverns takes place. Extensive plane strain finite difference analyses were carried out to examine the deformations induced by excavation of underground twin caverns. From the numerical results, a fairly simple nonparametric regression algorithm known as multivariate adaptive regression splines (MARS) has been used to relate the maximum key point displacement and the percent strain to various parameters including the rock quality, the cavern geometry and the in situ stress. Probabilistic assessments on the serviceability limit state of twin caverns can be performed using the First-order reliability spreadsheet method (FORM) based on the built MARS model. Parametric studies indicate that the probability of failure P_f increases as the coefficient of variation of Q increases, and P_f decreases with the widening of the pillar.

Keywords: serviceability limit state; the maximum key point displacement; twin caverns; percent strain; multivariate adaptive regression splines

1. Introduction

The construction of a new cavern near an existing cavern modifies the state of stresses and movements in a zone around the existing cavern. For multiple caverns, the size of this influence zone depends on the ground type, the in situ stress, the cavern span, the width of the pillar separating the caverns, and the excavation sequences. If two adjacent excavations are constructed far apart such that their influence zones do not overlap, then the individual cavern can be considered separately as single caverns and analyzed as such. However, if the influence zones of the twin caverns do overlap, some degree of interaction between the twin caverns will take place. Interaction of the twin caverns will affect the global stability, the state of stress and the deformations around the caverns. The ultimate limit state failure for stress-induced instability was usually assessed in terms of global factor of safety. However, the serviceability limit state, which denotes failure due to excessive movements, should also be considered. Thus an accurate estimation of the deformation induced by cavern excavation is necessary. Considering the uncertainties existing in the design parameters, the calculation on the probability of the cavern

*Corresponding author, Associate Professor, E-mail: ctcgoh@ntu.edu.sg
[a] Research Fellow, E-mail; zhangwg@ntu.edu.sg

http://www.techno-press.org/?journal=gae&subpage=7 ISSN: 2005-307X (Print), 2092-6219 (Online)

deformation exceeding the prescribed limiting value is important.

In this paper, plane strain finite difference analyses using FLAC^{3D} were performed in which the deformation of the twin parallel caverns is investigated. Based on the numerical results, this paper first describes the multivariate adaptive regression splines (MARS) response surface models developed for estimating the maximum key point displacement $u_{\max\_t}$ and the percent strains ε_t. This study then demonstrates how reliability analysis on the serviceability limit state of twin caverns can be performed using the First-order reliability method (FORM) to estimate the probability of the cavern deformation exceeding the prescribed limiting value.

2. Details of MARS

Friedman (1991) introduced MARS as a statistical method for fitting the relationship between a set of input variables and dependent variables. It is a nonlinear and nonparametric regression method based on a divide and conquer strategy in which the training data sets are partitioned into separate piecewise linear segments (splines) of differing gradients (slope). No specific assumption about the underlying functional relationship between the input variables and the output is required. The end points of the segments are called knots. A knot marks the end of one region of data and the beginning of another. The resulting piecewise curves (known as basis functions), give greater flexibility to the model, allowing for bends, thresholds, and other departures from linear functions.

MARS generates basis functions by searching in a stepwise manner. An adaptive regression algorithm is used for selecting the knot locations. MARS models are constructed in a two-phase procedure. The forward phase adds functions and finds potential knots to improve the performance, resulting in an overfit model. The backward phase involves pruning the least effective terms. An open source code on MARS from Jekabsons (2010) is used in carrying out the analyses presented in this paper.

Let $\boldsymbol{y}$ be the target output and $\boldsymbol{X} = (X_1, \ldots, X_P)$ be a matrix of P input variables. Then it is assumed that the data are generated from an unknown "true" model. In case of a continuous response this would be

$$y = f(X_1,\ldots,X_p) + e = f(\boldsymbol{X}) + e \tag{1}$$

in which e is the distribution of the error. MARS approximates the function f by applying basis functions (*BF*s). *BF*s are splines (smooth polynomials), including piecewise linear and piecewise cubic functions. For simplicity, only the piecewise linear function is expressed. Piecewise linear functions are of the form $\max(0, x - t)$ with a knot occurring at value t. The equation max(.) means that only the positive part of (.) is used otherwise it is given a zero value. Formally

$$\max(0, x-t) = \begin{cases} x-t, & \text{if} \quad x \geq t \\ 0, & \text{otherwise} \end{cases} \tag{2}$$

The MARS model $f(\boldsymbol{X})$, is constructed as a linear combination of *BF*s and their interactions, and is expressed as

$$f(\boldsymbol{X}) = \beta_0 + \sum_{m=1}^{M} \beta_m \lambda_m(\boldsymbol{X}) \tag{3}$$

where each $\lambda_m(\boldsymbol{X})$ is a basis function. It can be a spline function, or the product of two or more spline functions already contained in the model (higher orders can be used when the data warrants it; for simplicity, at most second-order is assumed in this paper). The coefficients β are constants, estimated using the least-squares method.

Fig. 1 shows a simple example of how MARS would use piecewise linear spline functions to attempt to fit data. The MARS mathematical equation is expressed as

$$y = -20.79 - 6.55 \times BF1 + 6.54 \times BF2 - 4.20 \times BF3 + 4.72 \times BF4 - 3.99 \times BF5 \tag{4}$$

where $BF1 = \max(0, x - 16)$, $BF2 = \max(0, 16 - x)$, $BF3 = \max(0, 14.5 - x)$, $BF4 = \max(0, x - 10)$ and $BF5 = \max(0, 5.5 - x)$. The knots are located at x = 5.5, 10, 14.5 and 16. They delimit five intervals where different linear relationships are identified.

The MARS modeling is a data-driven process. To fit the model in Eq. (3), first a forward selection procedure is performed on the training data. A model is constructed with only the intercept, β_0, and the basis pair that produces the largest decrease in the training error is added. Considering a current model with M basis functions, the next pair is added to the model in the form

$$\hat{\beta}_{M+1}\lambda_m(\boldsymbol{X})\max(0, X_j - t) + \hat{\beta}_{M+2}\lambda_m(\boldsymbol{X})\max(0, t - X_j) \tag{5}$$

with each β being estimated by the method of least squares. As a basis function is added to the model space, interactions between *BF*s that are already in the model are also considered. *BF*s are added until the model reaches some maximum specified number of terms leading to a purposely overfit model.

To reduce the number of terms, a backward deletion sequence follows. The aim of the backward deletion procedure is to find a close to optimal model by removing extraneous variables. The backward pass prunes the model by removing the *BF*s with the lowest contribution to the model until it finds the best sub-model. Thus, the *BF*s maintained in the final optimal model are

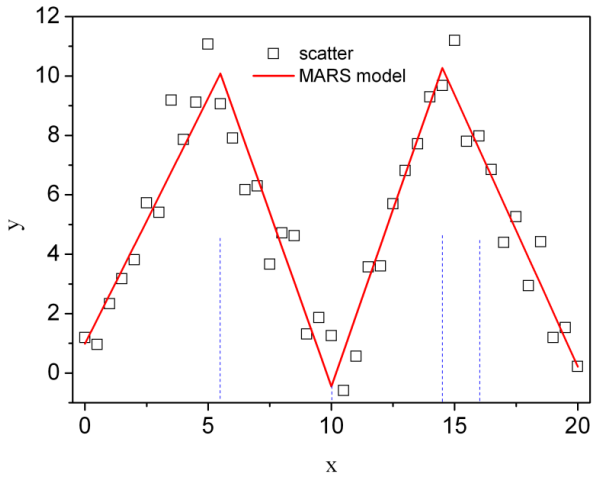

Fig. 1 Knots and linear splines for a simple MARS example

selected from the set of all candidate *BF*s, used in the forward selection step. Model subsets are compared using the less computationally expensive method of Generalized Cross-Validation (GCV). The GCV equation is a goodness of fit test that penalizes large numbers of *BF*s and serves to reduce the chance of overfitting. For the training data with *N* observations, GCV for a model is calculated as follows (Hastie *et al*. 2009)

$$\mathrm{GCV} = \frac{\frac{1}{N}\sum_{i=1}^{N}\left[y_i - f(x_i)\right]^2}{\left[1 - \frac{M + d \times (M-1)/2}{N}\right]^2} \tag{6}$$

in which *M* is the number of *BF*s, *d* is the penalizing parameter, *N* is the number of observations, and $f(x_i)$ denotes the predicted values of the MARS model. The numerator is the mean squared error of the evaluated model in the training data, penalized by the denominator. The denominator accounts for the increasing variance in the case of increasing model complexity. Note that $(M - 1)/2$ is the number of hinge function knots. The GCV penalizes not only the number of the model's basis functions but also the number of knots. A default value of 3 is assigned to penalizing parameter *d* (Friedman 1991). At each deletion step a basis function is removed to minimize Eq. (3), until an adequately fitted model is found. MARS is an adaptive procedure because the selection of *BF*s and the variable knot locations are data-based and specific to the problem at hand.

After the optimal MARS model is determined, by grouping together all the *BF*s that involve one variable and another grouping of *BF*s that involve pairwise interactions (and even higher level interactions when applicable), the procedure known as analysis of variance (ANOVA) decomposition (Friedman 1991) can be used to assess the contributions from the input variables and the *BF*s. Previous applications of MARS algorithm in civil engineering can be found in Attoh-Okine *et al*. (2009), Lashkari (2012), Mirzahosseinia *et al*. (2011), Zarnani *et al*. (2011), Samui (2011), Samui and Karup (2011), Zhang and Goh (2013), Goh and Zhang (2014) and Goh *et al*. (2013). However, use of MARS in underground excavations is limited.

3. Numerical modeling

The FLAC^{3D} code (Itasca 2005) was utilized for the numerical experiments. The assumptions of the numerical analysis, the cross-section layout of the twin caverns, and the basic design parameters used are described in this section.

3.1 Assumptions of numerical analysis

The basic assumptions of numerical analyses in this case are:

(1) the study was a two-dimensional plane strain problem;
(2) the discontinuous nature of the rock is incorporated implicitly in the Mohr-Coulomb constitutive relationship used to represent the mass as an equivalent continuum;
(3) the rock material obeyed Mohr-Coulomb failure criterion that follows the elastic perfectly-lastic stress-strain relationship;
(4) the caverns are unsupported;
(5) the twin caverns are of equal size, both horse-shoe shaped, with semi-circular roof, the

span-to-side wall height ratio (B/H) is 2, and horizontally aligned;

(6) the excavation involves six stages: heading, first benching, second benching of the right cavern, followed by heading, first benching, second benching of the left cavern;

(7) the effect of creep was not considered in the analysis.

It is accepted that a three-dimensional analysis would more realistically account for the longitudinal effects of the face advancement. However, the aim of this study is to provide engineers with preliminary estimates of the expected maximum cavern displacements and the percent strain during construction, hence the simpler plane strain analyses have been carried out.

3.2 Cross-section layout

One significant parameter influencing the interaction is the cavern span B. In this study, B values of 10, 20 and 30 m are considered. In the numerical models, the cavern crown is 65 m below the ground surface. The plane-strain conditions are enforced by including a thin 1 m slice of material in the longitudinal direction and imposing boundary conditions on the two off-plane surfaces that allow movement vertically but are restrained against displacements normal to these planes. Outer boundaries are located far from the cavern wall. No surface loading above-ground surface is considered. The initial vertical in situ stress σ_v is induced by self-weight of the rock. The physical and geometrical model including the twin caverns and the design variables considered are shown in Fig. 2.

3.3 Ranges of design parameters

The main factors affecting interaction between the twin caverns are found to be the cavern geometry, the rock mass strength properties, the in situ stress field, and the excavation sequence. While the effects of some of the factors such as the strength properties and the in situ stresses are

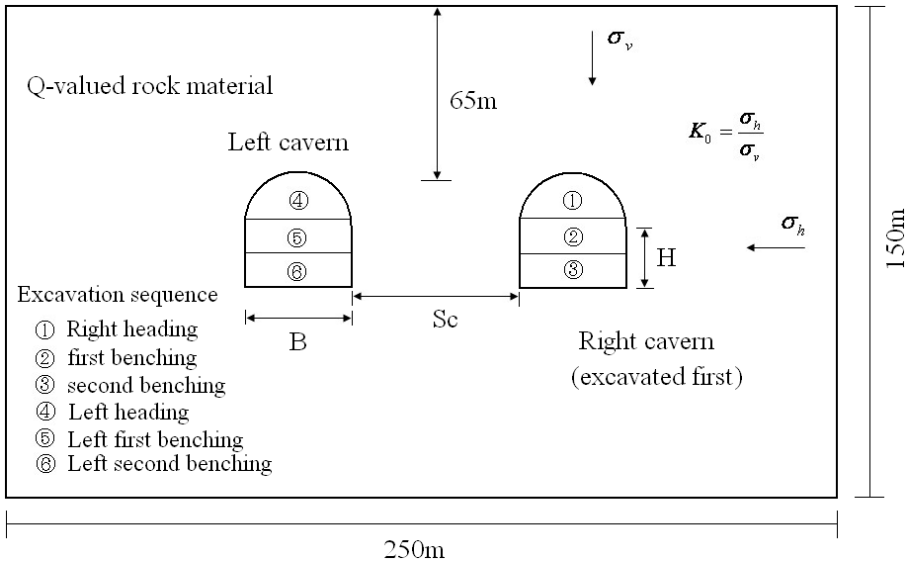

Fig. 2 Geometrical model and basic design parameters

Table 1 Cavern design parameters

Parameter	Description	Values
K_0	In situ stress ratio	0.5, 1, 2
B	Cavern span (m)	10, 20, 30
S_c/B	Ratio of pillar width to cavern span	1, 1.5, 2, 2.5
Q	Tunneling quality index	1, 4, 10, 40, 100

measurable, the effects of the others such as excavation sequence cannot be quantified. For simplicity, excavation in six stages as described in Fig. 2 is regarded as deterministic. The other important factors are shown in Table 1.

For the numerical analyses, the rock mass properties are indirectly (through *RMR*) determined from the *Q* system by means of commonly used empirical equations and correlations.

3.4 Determination of rock mass strength parameters

In the preliminary stage of an engineering design, the need for an approximate estimate of the rock mass parameters frequently arises (Barton *et al*. 1980, Hoek and Brown 1997, Basarir 2006, Aksoy *et al*. 2010). For the numerical analyses carried out in this study, the following equations (Eqs. (7)-(13)) are adopted for determining the rock mass properties.

$$RMR = 7\ln Q + 36 \qquad \text{(Tugrul 1998)} \tag{7}$$

$$E_m(\text{GPa}) = 10^{(RMR-10)/40} (RMR < 50) \qquad \text{(Serafim and Pereira 1983)} \tag{8}$$

$$E_m(\text{GPa}) = 2RMR - 100 (RMR > 50) \qquad \text{(Bieniawski 1978)} \tag{9}$$

$$c(\text{MPa}) = 0.005(RMR - 1.0) \qquad \text{(Bieniawski 1989)} \tag{10}$$

$$\phi(^\circ) = 0.05RMR + 4.5 \qquad \text{(Bieniawski 1989)} \tag{11}$$

$$\sigma_{cm}(\text{MPa}) = RMR \qquad \text{(Palmstrom 2000)} \tag{12}$$

$$\sigma_t(\text{MPa}) = \sigma_{cm}/10 \tag{13}$$

where E_m is the deformation modulus of rock mass, c is the cohesive strength, ϕ is the internal friction angle, σ_{cm} is the Uniaxial Compressive Strength (*UCS*) of rock material and σ_t is the tensile strength. Adopting the above empirical equations, the Q value of each category and its corresponding Mohr-Coulomb rock properties to be used in the numerical calculations are shown in Table 2. In Table 2, the Poisson's ratio μ values are assumed. For simplicity, density of 2670 kg / m^3 is assumed for rock mass of all the ranges of Q. Similar correlations were used for the analysis of single caverns (Goh and Zhang 2012).

Table 2 Rock mass properties with different Q values

Q	c (MPa)	ϕ (°)	E_m (GPa)	μ	σ_t (MPa)
1	0.18	22.5	4.47	0.35	2.40
4	0.22	27.4	7.81	0.20	3.05
10	0.26	30.6	11.30	0.20	3.47
40	0.30	35.4	19.75	0.16	4.12
100	0.34	38.6	28.57	0.16	4.55

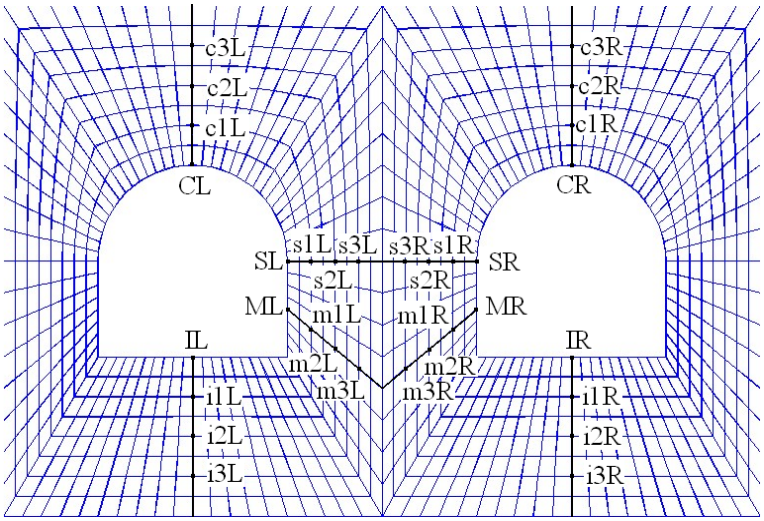

Fig. 3 Details of cavern peripheral nodes between twin caverns

3.5 Determination of the maximum key point displacements and the percent strains

During construction, the displacements of the key points around the cavern like the crown or the invert are usually continuously monitored. Based on the magnitude and the changing trend of these key point displacements, the stability of excavations is assessed. In this section, the influences of S_c/B, Q, B and K_0 on key point displacements of the twin caverns are investigated. These key points include the crown, the springline, the middle side wall, and the invert of the right cavern and of the left cavern, denoted as *CR*, *SR*, *MR*, *IR*, *CL*, *SL*, *ML* and *IL* respectively. $u_{\max\_t}$ is defined as max(u_{CR}, u_{SR}, u_{MR}, u_{IR}, u_{CL}, u_{SL}, u_{ML}, u_{IL}), in which u_{CR}, u_{SR}, u_{MR}, and u_{IR} are the displacements of peripheral nodes *C*, *S*, *M* and *I* of the right cavern (which is excavated first), respectively, while u_{CL}, u_{SL}, u_{ML}, and u_{IL} are the displacements of peripheral nodes *C*, *S*, *M* and *I* of the left cavern, as shown in Fig. 3. A similar approach was adopted to assess the deformations and strains for single caverns (Zhang and Goh 2012).

The strain value in each of the key points, take ε_{CR} for example, is

$$\varepsilon_{CR} = \max(\varepsilon_{CR\_c1R}, \quad \varepsilon_{CR\_c2R}, \quad \varepsilon_{CR\_c3R}) \tag{14}$$

in which ε_{CR_ciR} (i = 1, 2, 3) is defined as

$$\varepsilon_{CR\_ciR}(\%) = \frac{u_{CR} - u_{ciR}}{l_{CR\_ciR}} \times 10 \tag{15}$$

where u_{ciR} is the displacement of the corresponding inner node *ciR* and l_{CR_ciR} is the length between nodes *CR* and *ciR* (Fig. 3).

The percent strain of the twin caverns ε_t is the maximum of the strains of the eight key points

$$\varepsilon_t = \max(\varepsilon_{CR}, \varepsilon_{SR}, \varepsilon_{MR}, \varepsilon_{IR}, \varepsilon_{CL}, \varepsilon_{SL}, \varepsilon_{ML}, \varepsilon_{IL}) \tag{16}$$

As illustrated in Fig. 3, the displacements of 32 nodes are obtained from the numerical analyses from which the percent strain is determined.

4. Modeling results and analyses of u_{max_t}

4.1 Change of the key displacements with excavation stages

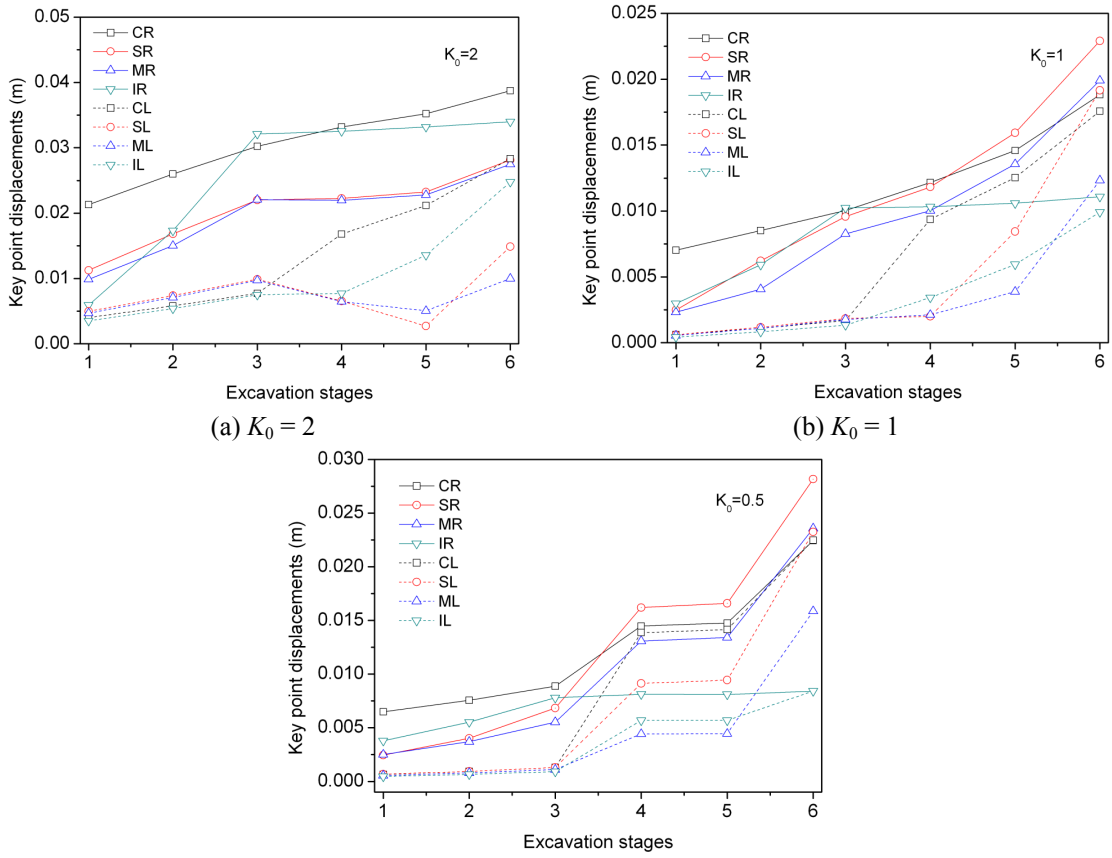

(a) $K_0 = 2$ (b) $K_0 = 1$

(c) $K_0 = 0.5$

Fig. 4 Key point displacements with excavation stage for $S_c/B = 1.5$, $Q = 4$, $B = 20$ m: (a) $K_0 = 2$; (b) $K_0 = 1$, and (c) $K_0 = 0.5$

Fig. 4(a)-(c) shows the key point displacement with the excavation stages for the case of S_c/B = 1.5, Q = 4, B = 20 m under K_0 = 2, 1, and 0.5 respectively. It can be observed that under high in situ stress ratio (K_0 = 2), the key point displacements are relatively larger than those for K_0 = 1 and 0.5. The largest key point displacement is about 0.04 m and occurs at the crown of the first (right) excavated cavern. It is also clear that large displacements of the key points around the right cavern have already occurred before the start of the left cavern excavation (stage 4) as a result of a high

Table 3 u_{max_t} (m) for B = 10 m

Q	K_0	S_c/B				u_{max_s}
		1	1.5	2	2.5	
1	0.5	0.031	0.030	0.026	0.020	0.010
	1	0.030	0.028	0.025	0.019	0.014
	2	0.093	0.078	0.067	0.061	0.058
4	0.5	0.009	0.006	0.004	0.004	0.004
	1	0.009	0.006	0.005	0.005	0.005
	2	0.019	0.018	0.017	0.016	0.016
10	0.5	0.003	0.002	0.002	0.002	0.002
	1	0.003	0.003	0.003	0.003	0.003
	2	0.009	0.008	0.007	0.007	0.007
40	0.5	0.001	0.001	0.001	0.001	0.001
	1	0.001	0.001	0.001	0.001	0.001
	2	0.003	0.003	0.003	0.002	0.003
100	0.5	0.001	0.001	0.001	0.001	0.001
	1	0.001	0.001	0.001	0.001	0.001
	2	0.002	0.001	0.001	0.001	0.002

Table 4 u_{max_t} (m) for B = 20 m

Q	K_0	S_c/B				u_{max_s}
		1	1.5	2	2.5	
4	0.5	–	0.028	0.013	0.011	0.009
	1	–	0.023	0.013	0.012	0.010
	2	–	0.039	0.036	0.034	0.033
10	0.5	0.012	0.007	0.006	0.005	0.005
	1	0.012	0.007	0.006	0.006	0.006
	2	0.017	0.016	0.015	0.014	0.016
40	0.5	0.003	0.003	0.002	0.002	0.002
	1	0.003	0.003	0.002	0.002	0.002
	2	0.007	0.006	0.006	0.005	0.006
100	0.5	0.002	0.002	0.002	0.002	0.002
	1	0.002	0.002	0.002	0.002	0.002
	2	0.003	0.003	0.003	0.003	0.004

Table 5 u_{max_t} (m) for B = 30 m

Q	K_0	S_c/B				u_{max_s}
		1	1.5	2	2.5	
4	0.5	–	–	0.027	0.019	0.018
	1	–	–	0.025	0.021	0.018
	2	–	–	0.061	0.054	0.047
10	0.5	0.033	0.011	0.009	0.008	0.008
	1	0.017	0.011	0.009	0.009	0.007
	2	0.027	0.023	0.020	0.019	0.020
40	0.5	0.005	0.004	0.004	0.004	0.004
	1	0.004	0.004	0.003	0.003	0.003
	2	0.008	0.008	0.008	0.007	0.008
100	0.5	0.003	0.002	0.002	0.002	0.002
	1	0.002	0.002	0.002	0.002	0.002
	2	0.004	0.004	0.004	0.004	0.005

horizontal stress release during excavation. For the cases with K_0 = 1 and 0.5, displacements of the key points around the left cavern are small before stage 4 and for these two cases, the largest displacement occurs at the springline of the first excavated cavern.

4.2 Modeling results of u_{max_t}

Tables 3-5 list the u_{max_t} of the numerical cases with global factor of safety greater than 1.0 for B = 10, 20, and 30 m, respectively. For these cases, the deformed meshes are not seriously distorted. The last column also includes the maximum key point displacement of a single cavern u_{max_s} for comparison.

The influence of pillar geometry S_c/B on u_{max_t}, is clearly evident from Tables 3-5. The greatest difference between excavation of single cavern and the twin caverns lies in the fact that, for the latter, the excavation of the left cavern influences deformation of the right cavern as a result of significant interaction between the twin caverns. It is obvious that generally with increase of S_c/B, u_{max_t} converges to u_{max_s}, indicating that the interaction attenuates as S_c/B increases. For different cases, interaction diminishes at different S_c/B values. However, in all cases, interaction is considerable for a S_c/B value of 1.0. u_{max_t} decreases as Q increases since higher Q corresponds to greater deformation modulus and increased strength of the rock mass. In addition, for the same Q value, u_{max_t} is significantly influenced by K_0. For each plot, the u_{max_t} value for K_0 = 2 is much higher than those for K_0 = 1 and K_0 = 0.5 since higher K_0 value results in larger horizontal stress release during excavation.

4.3 Determination of u_{max_t} using MARS

Based on the data listed in Tables 3-5, the MARS model for u_{max_t} was built. Of the 147 observations, 109 patterns were randomly selected as the training data and the remaining 38 data were used for testing. The training data sets are listed in Table 6. The MARS testing patterns are

Table 6 Training data results of MARS model for u_{max_t}

B (m)	Q	K_0	S_c	$u_{max\_t\_FDM}$ (mm)	$u_{max\_t\_MARS}$ (mm)	B (m)	Q	K_0	S_c	$u_{max\_t\_FDM}$ (mm)	$u_{max\_t\_MARS}$ (mm)
10	1	0.5	1	30.4	34.7	20	10	1	2	5.9	4.1
10	1	0.5	2	25.8	22.0	20	10	1	2.5	5.5	2.9
10	1	0.5	2.5	19.6	16.8	20	10	2	1	17.4	16.6
10	1	1	1	29.6	34.7	20	10	2	1.5	15.9	10.6
10	1	1	1.5	28.2	27.2	20	10	2	2.5	14.1	8.3
10	1	1	2.5	18.6	16.8	20	40	0.5	1	3.2	4.5
10	1	2	1	92.8	84.0	20	40	0.5	2	2.5	3.3
10	1	2	2	67.2	71.2	20	40	0.5	2.5	2.4	2.2
10	1	2	2.5	61.2	66.0	20	40	1	1	2.9	4.5
10	4	0.5	1	9.3	6.9	20	40	1	1.5	2.6	4.5
10	4	0.5	1.5	6.2	4.1	20	40	1	2.5	2.4	2.2
10	4	0.5	2.5	4.1	1.8	20	40	2	1	6.6	4.5
10	4	1	1	9.5	6.9	20	40	2	2	5.7	3.3
10	4	1	2	5.2	3.0	20	40	2	2.5	5.3	2.2
10	4	1	2.5	5.0	1.8	20	100	0.5	1	1.8	3.0
10	4	2	1	19.0	25.2	20	100	0.5	1.5	1.6	3.0
10	4	2	1.5	17.8	22.4	20	100	0.5	2.5	1.6	0.7
10	4	2	2.5	16.2	20.1	20	100	1	1	1.7	3.0
10	10	0.5	1	3.4	6.8	20	100	1	2	1.5	1.8
10	10	0.5	2	2.3	4.1	20	100	1	2.5	1.5	0.7
10	10	0.5	2.5	2.3	2.9	20	100	2	1	3.4	3.0
10	10	1	1	3.2	6.8	20	100	2	1.5	3.1	3.0
10	10	1	1.5	2.8	5.2	20	100	2	2.5	2.8	0.7
10	10	1	2.5	2.5	2.9	30	4	0.5	2.5	19.2	24.5
10	10	2	1	8.5	12.2	30	4	1	2	24.6	25.7
10	10	2	2	7.4	9.5	30	4	1	2.5	21.0	24.5
10	10	2	2.5	7.0	8.3	30	4	2	2	60.9	48.3
10	40	0.5	1	1.3	0.1	30	10	0.5	1	33.2	19.1
10	40	0.5	1.5	1.2	4.5	30	10	0.5	2	9.0	12.0
10	40	0.5	2.5	1.2	2.2	30	10	0.5	2.5	8.3	10.8
10	40	1	1	1.3	0.1	30	10	1	1	16.9	19.1
10	40	1	2	1.2	3.3	30	10	1	1.5	10.7	13.1
10	40	1	2.5	1.1	2.2	30	10	1	2.5	8.5	10.8
10	40	2	1	3.0	0.1	30	10	2	1	27.0	28.8
10	40	2	1.5	2.7	4.5	30	10	2	2	20.3	21.6
10	40	2	2.5	2.3	2.2	30	10	2	2.5	18.8	20.5
10	100	0.5	1	0.9	-1.4	30	40	0.5	1	4.7	4.5
10	100	0.5	2	0.8	1.8	30	40	0.5	1.5	4.2	4.5
10	100	0.5	2.5	0.8	0.7	30	40	0.5	2.5	3.6	2.2

Table 6 Continued

B (m)	Q	K_0	S_c	$u_{max\_t\_FDM}$ (mm)	$u_{max\_t\_MARS}$ (mm)	B (m)	Q	K_0	S_c	$u_{max\_t\_FDM}$ (mm)	$u_{max\_t\_MARS}$ (mm)
10	100	1	1	0.8	-1.4	30	40	1	1	4.1	4.5
10	100	1	1.5	0.8	3.0	30	40	1	2	3.4	3.3
10	100	1	2.5	0.7	0.7	30	40	1	2.5	3.4	2.2
10	100	2	1	1.5	-1.4	30	40	2	1	7.8	8.8
10	100	2	2	1.3	1.8	30	40	2	1.5	8.1	8.8
10	100	2	2.5	1.2	0.7	30	40	2	2.5	7.1	6.5
20	4	0.5	2	13.0	16.2	30	100	0.5	1	2.7	3.0
20	4	0.5	2.5	10.8	15.1	30	100	0.5	2	2.3	1.8
20	4	1	1.5	22.9	17.4	30	100	0.5	2.5	2.3	0.7
20	4	1	2.5	12.2	15.1	30	100	1	1	2.3	3.0
20	4	2	2	35.9	34.5	30	100	1	1.5	2.2	3.0
20	4	2	2.5	34.3	33.4	30	100	1	2.5	2.1	0.7
20	10	0.5	1	12.4	11.2	30	100	2	1	4.1	7.3
20	10	0.5	1.5	6.6	5.2	30	100	2	2	3.9	6.1
20	10	0.5	2.5	5.4	2.9	30	100	2	2.5	3.7	5.0
20	10	1	1	12.0	11.2						

Table 7 Testing data sets of MARS model for u_{max_t}

B (m)	Q	K_0	S_c	$u_{max\_t\_FDM}$ (mm)	$u_{max\_t\_MARS}$ (mm)	B (m)	Q	K_0	S_c	$u_{max\_t\_FDM}$ (mm)	$u_{max\_t\_MARS}$ (mm)
10	1	0.5	15	30.9	27.2	20	10	1	30	6.6	5.2
10	1	1	20	24.9	22.0	20	10	2	40	14.9	9.5
10	1	2	15	78.4	76.5	20	40	0.5	30	2.7	4.5
10	4	0.5	20	4.5	3.0	20	40	1	40	2.5	3.3
10	4	1	15	5.8	4.1	20	40	2	30	6.0	4.5
10	4	2	20	17.1	21.3	20	100	0.5	40	1.6	1.8
10	10	0.5	15	2.5	5.2	20	100	1	30	1.6	3.0
10	10	1	20	2.7	4.1	20	100	2	40	2.9	1.8
10	10	2	15	7.9	10.6	30	4	0.5	60	27.1	25.7
10	40	0.5	20	1.2	3.3	30	4	2	75	53.6	47.2
10	40	1	15	1.2	4.5	30	10	0.5	45	11.1	13.1
10	40	2	20	2.5	3.3	30	10	1	60	9.2	12.0
10	100	0.5	15	0.8	3.0	30	10	2	45	22.7	22.8
10	100	1	20	0.7	1.8	30	40	0.5	60	3.8	3.3
10	100	2	15	1.4	3.0	30	40	1	45	3.8	4.5
20	4	0.5	30	28.2	17.4	30	40	2	60	7.5	7.6
20	4	1	40	13.3	16.2	30	100	0.5	45	2.5	3.0
20	4	2	30	38.7	35.7	30	100	1	60	2.2	1.8
20	10	0.5	40	5.7	4.1	30	100	2	45	4.2	7.3

shown in Table 7. To eliminate unnecessary rounding errors, the units of $u_{\max\_t}$ is changed from meters (m) to millimeters (mm). The same units are also used for the MARS model predictions in Eq. (17).

The optimal MARS model consisted of 13 *BF*s of linear spline functions with second-order interaction. A plot of $u_{\max\_t\_\mathrm{MARS}}$ versus $u_{\max\_t\_\mathrm{FDM}}$ shown in Fig. 5 indicates that the built MARS model is reasonably accurate. Error measures in Rows 2-4 of Table 8 indicate that the MARS $u_{\max\_t}$ model predictions are satisfactory in terms of accuracy.

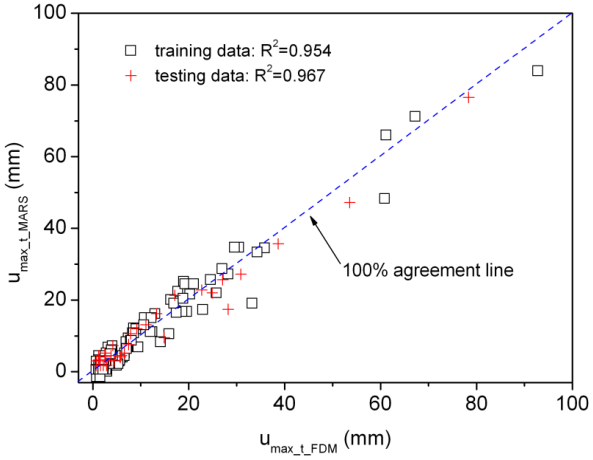

Fig. 5 Comparison between $u_{\max\ t\ \mathrm{MARS}}$ and $u_{\max\ t\ \mathrm{FDM}}$

Table 8 Error measures used for MARS models

MARS models		Relative root mean squared error *RRMSE* (%)	Correlation coefficient *r*	Performance index ρ
$u_{\max\_t}$	Training	25.5	0.977	0.129
	Testing	12.6	0.986	0.063
	overall	28.2	0.979	0.143
ε_t	Training	9.56	0.997	0.048
	Testing	6.30	0.997	0.032
	overall	11.5	0.997	0.057

Note:

$$RRMSE = \frac{\frac{1}{N}\sum_{i=1}^{N}(Y_i - y_i)^2}{\frac{1}{N}\sum_{i=1}^{N} y_i} \times 100 \quad r = \frac{\sum_{i=1}^{N}(Y_i - \bar{Y})(y_i - \bar{y})}{\sqrt{\sum_{i=1}^{N}(Y_i - \bar{Y})^2}\sqrt{\sum_{i=1}^{N}(y_i - \bar{y})^2}} \times 100 \quad \rho = \frac{RRMSE}{1 + r}$$

$\bar{y}$ is the mean of the target values of y_i; $\bar{Y}$ is the mean of the predicted Y_i; N denotes the number of data points in the used set, training set, testing set or the overall set;
Definitions of *RRMSE*, *r* and ρ are based on Gandomi and Roke (2013)

Table 9 ANOVA decomposition of the developed MARS model for u_{max_t}

Functions	GCV	STD	#basis	variable(s)
1	305.8	10.23	3	Q
2	23.3	1.02	1	S_c/B
3	168.0	8.97	3	Q, K_0
4	47.9	3.81	2	Q, S_c/B
5	120.0	7.29	2	Q, B
6	22.5	1.25	1	K_0, B
7	24.3	1.50	1	B, S_c/B

Table 9 displays the ANOVA decomposition of the developed MARS model. The first column in Table 9 lists the ANOVA function number. The second column gives an indication of the importance of the corresponding ANOVA function, by listing the GCV score for a model with all *BF*s corresponding to that particular ANOVA function removed. This GCV score can be used to evaluate whether the ANOVA function is making an important contribution to the model, or whether it just slightly helps to improve the global GCV score. The third column provides the standard deviation of this function. The fourth column gives the number of *BF*s comprising the ANOVA function. The last column gives the particular input variables associated with the ANOVA function. The parameter relative importance can be evaluated by the increase in the GCV value caused by removing the considered variables from the developed MARS model. It is obvious that u_{max_t} is mainly influenced by Q, followed by S_c/B. u_{max_t} is also significantly influenced by the interaction terms Q and K_0 (Function 3), and Q and B (Function 5).

Table 10 lists the *BF*s of the MARS model and their corresponding equations. The interpretable MARS model to predict u_{max_t} is given by

Table 10 *BF*s and corresponding equations of MARS model for u_{max_t}

*BF*s	Equation
*BF*1	$\max(0, Q - 4)$
*BF*2	$\max(0, 4 - Q)$
*BF*3	$BF2 \times \max(0, K_0 - 1)$
*BF*4	$\max(0, Q - 10)$
*BF*5	$\max(0, 10 - Q) \times \max(0, K_0 - 1)$
*BF*6	$\max(0, B - 20) \times \max(0, 40 - Q)$
*BF*7	$BF2 \times \max(0, 2.5 - S_c/B)$
*BF*8	$\max(0, 20 - B) \times \max(0, 10 - Q)$
*BF*9	$\max(0, B - 20) \times \max(0, K_0 - 1)$
*BF*10	$\max(0, S_c/B - 1.5)$
*BF*11	$\max(0, 1.5 - S_c/B) \times \max(0, 40 - Q)$
*BF*12	$\max(0, 1.5 - S_c/B) \times \max(0, 20 - B)$
*BF*13	$\max(0, K_0 - 1) \times \max(0, 40 - Q)$

$$\begin{aligned} & u_{\max\_t\_MARS}(\text{mm}) \\ & = 17.35 - 2.023 \times BF1 + 7.193 \times BF2 + 8.151 \times BF3 + 1.998 \times BF4 \\ & \quad + 1.975 \times BF5 + 0.026 \times BF6 + 2.726 \times BF7 - 0.221 \times BF8 + 0.430 \\ & \quad \times BF9 - 2.281 \times BF10 + 0.397 \times BF11 - 0.869 \times BF12 + 0.180 \times BF13 \end{aligned} \tag{17}$$

This $u_{\max\_t}$ equation can be used to provide preliminary estimates of the expected maximum cavern displacements during construction of the twin caverns.

5. Modeling results and analyses of ε_t

5.1 Modeling results of ε_t

Table 11 lists the percent strains for the 147 observations. Based on the ε_t values in Table 11, Fig. 6 presents some typical plots of the influence of pillar geometry S_c/B on the percent strains, compared with the single cavern case. Generally ε_t decreases with the increase of S_c/B and converges to the value of the single cavern case, which indicates that the interaction between the twin caverns attenuates with increasing of spacing. For different cases, interaction diminishes at different S_c/B values. ε_t is also significantly influenced by K_0. For each plot, the ε_t value for $K_0 = 2$ is much greater than those for $K_0 = 1$ and $K_0 = 0.5$, because of the larger horizontal stress release during cavern excavation.

Table 11 Percent strains ε_t of the 147 observations (%)

Q	K_0	B = 10 m				B = 20 m				B = 30 m			
		S_c/B = 0.25	0.5	1	2	0.25	0.5	1	2	0.25	0.5	1	2
1	0.5	0.407	0.348	0.286	0.234	–	–	–	–	–	–	–	–
	1	0.366	0.322	0.305	0.271	–	–	–	–	–	–	–	–
	2	1.171	1.087	0.989	0.938	–	–	–	–	–	–	–	–
4	0.5	0.164	0.099	0.075	0.080	–	0.168	0.091	0.080	–	–	0.113	0.119
	1	0.160	0.095	0.095	0.094	–	0.133	0.088	0.087	–	–	0.106	0.123
	2	0.380	0.373	0.363	0.358	–	0.358	0.355	0.354	–	–	0.314	0.310
10	0.5	0.078	0.043	0.035	0.041	0.098	0.047	0.034	0.035	0.160	0.047	0.039	0.049
	1	0.066	0.049	0.049	0.048	0.094	0.047	0.047	0.046	0.084	0.047	0.051	0.061
	2	0.190	0.185	0.184	0.183	0.187	0.186	0.183	0.180	0.248	0.173	0.170	0.166
40	0.5	0.021	0.016	0.014	0.015	0.021	0.014	0.013	0.013	0.022	0.015	0.015	0.019
	1	0.024	0.020	0.019	0.019	0.023	0.021	0.021	0.021	0.031	0.021	0.022	0.028
	2	0.081	0.080	0.078	0.076	0.080	0.077	0.074	0.075	0.106	0.076	0.075	0.077
100	0.5	0.010	0.008	0.008	0.008	0.008	0.008	0.008	0.008	0.014	0.009	0.009	0.010
	1	0.012	0.010	0.010	0.010	0.013	0.012	0.012	0.012	0.017	0.012	0.013	0.017
	2	0.045	0.043	0.041	0.040	0.043	0.042	0.043	0.044	0.062	0.043	0.044	0.045

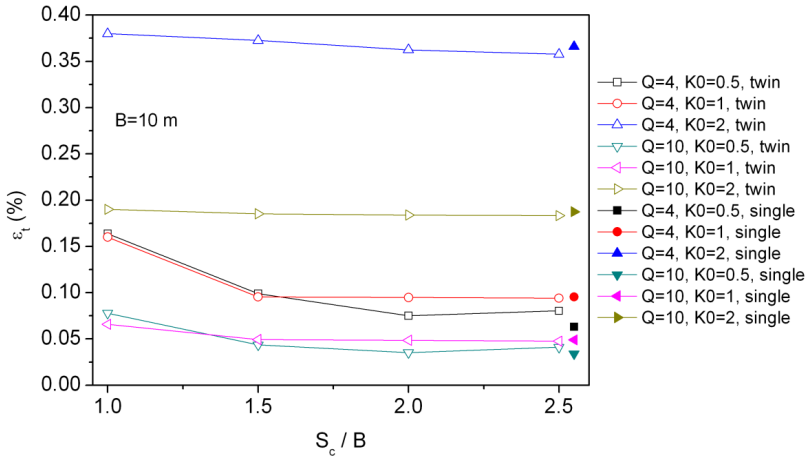

(a) B = 10 m

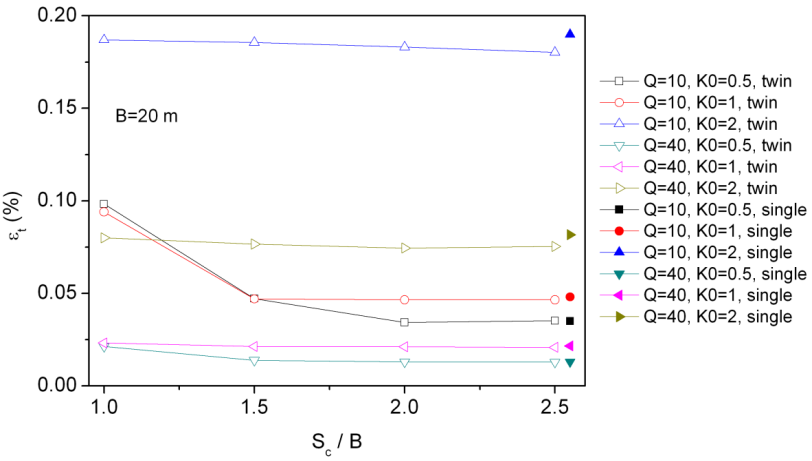

(b) B = 20 m

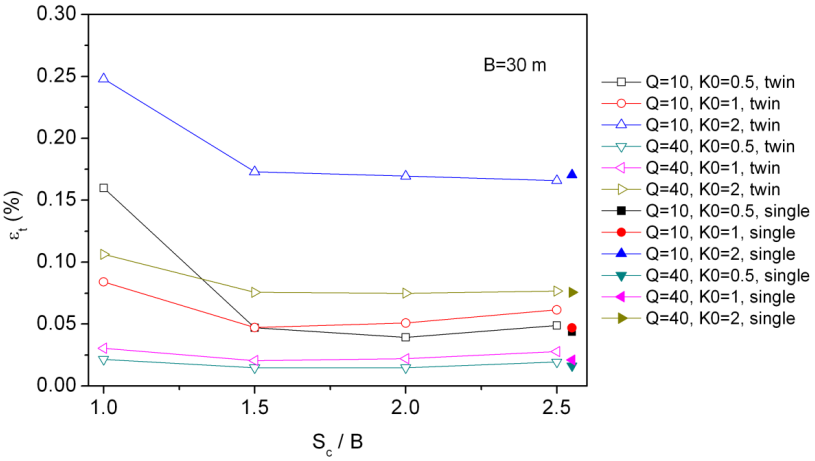

(c) B = 30 m

Fig. 6 Influence of S_c/B on ε_t: (a) B =10 m; (b) B = 20 m; and (c) B = 30 m

5.2 Determination of ε_t using MARS

MARS model was built to relate ε_t to the parameters Q, S_c/B, K_0 and B, using the data sets in Table 11. Of the 147 observations, 109 patterns were randomly selected as the training data and the remaining 38 data were used for testing. The optimal MARS model adopted 12 *BF*s of linear spline functions with second-order interaction. The training data sets and the corresponding MARS predictions are listed in Table 12. The MARS testing results are shown in Table 13. A plot of the $\varepsilon_{t\_\mathrm{MARS}}$ versus $\varepsilon_{t\_\mathrm{FDM}}$ is shown in Fig. 7. The high R^2 values and error measures in Rows 5-7 of Table 8 indicates that the MARS predictions are reasonably accurate.

Table 12 Training data results of ε_t for MARS

B (m)	Q	K_0	S_c	$\varepsilon_{t\_\mathrm{FDM}}$ (%)	$\varepsilon_{t\_\mathrm{MARS}}$ (%)	B (m)	Q	K_0	S_c	$\varepsilon_{t\_\mathrm{FDM}}$ (%)	$\varepsilon_{t\_\mathrm{MARS}}$ (%)
10	1	0.5	1	0.407	0.401	20	10	1	2	0.047	0.044
10	1	0.5	2	0.286	0.274	20	10	1	2.5	0.046	0.044
10	1	0.5	2.5	0.234	0.236	20	10	2	1	0.187	0.210
10	1	1	1	0.366	0.401	20	10	2	1.5	0.186	0.190
10	1	1	1.5	0.322	0.338	20	10	2	2.5	0.180	0.170
10	1	1	2.5	0.271	0.236	20	40	0.5	1	0.021	0.018
10	1	2	1	1.171	1.130	20	40	0.5	2	0.013	0.018
10	1	2	2	0.989	1.003	20	40	0.5	2.5	0.013	0.018
10	1	2	2.5	0.938	0.965	20	40	1	1	0.023	0.018
10	4	0.5	1	0.164	0.147	20	40	1	1.5	0.021	0.018
10	4	0.5	1.5	0.099	0.123	20	40	1	2.5	0.021	0.018
10	4	0.5	2.5	0.080	0.099	20	40	2	1	0.080	0.078
10	4	1	1	0.160	0.147	20	40	2	2	0.074	0.078
10	4	1	2	0.095	0.099	20	40	2	2.5	0.075	0.078
10	4	1	2.5	0.094	0.099	20	100	0.5	1	0.008	0.009
10	4	2	1	0.380	0.395	20	100	0.5	1.5	0.008	0.009
10	4	2	1.5	0.373	0.371	20	100	0.5	2.5	0.008	0.009
10	4	2	2.5	0.358	0.347	20	100	1	1	0.013	0.009
10	10	0.5	1	0.078	0.083	20	100	1	2	0.012	0.009
10	10	0.5	2	0.035	0.044	20	100	1	2.5	0.012	0.009
10	10	0.5	2.5	0.041	0.044	20	100	2	1	0.043	0.043
10	10	1	1	0.066	0.083	20	100	2	1.5	0.042	0.043
10	10	1	1.5	0.049	0.063	20	100	2	2.5	0.044	0.043
10	10	1	2.5	0.048	0.044	30	4	0.5	2.5	0.119	0.099
10	10	2	1	0.190	0.210	30	4	1	2	0.106	0.099
10	10	2	2	0.184	0.170	30	4	1	2.5	0.123	0.099
10	10	2	2.5	0.183	0.170	30	4	2	2	0.314	0.347
10	40	0.5	1	0.021	0.018	30	10	0.5	1	0.160	0.105

Table 12 Continued

B (m)	Q	K_0	S_c	ε_{t_FDM} (%)	ε_{t_MARS} (%)	B (m)	Q	K_0	S_c	ε_{t_FDM} (%)	ε_{t_MARS} (%)
10	40	0.5	1.5	0.016	0.018	30	10	0.5	2	0.039	0.044
10	40	0.5	2.5	0.015	0.018	30	10	0.5	2.5	0.049	0.044
10	40	1	1	0.024	0.018	30	10	1	1	0.084	0.105
10	40	1	2	0.019	0.018	30	10	1	1.5	0.047	0.063
10	40	1	2.5	0.019	0.018	30	10	1	2.5	0.061	0.044
10	40	2	1	0.081	0.078	30	10	2	1	0.248	0.232
10	40	2	1.5	0.080	0.078	30	10	2	2	0.170	0.170
10	40	2	2.5	0.076	0.078	30	10	2	2.5	0.166	0.170
10	100	0.5	1	0.010	0.009	30	40	0.5	1	0.022	0.039
10	100	0.5	2	0.008	0.009	30	40	0.5	1.5	0.015	0.018
10	100	0.5	2.5	0.008	0.009	30	40	0.5	2.5	0.019	0.018
10	100	1	1	0.012	0.009	30	40	1	1	0.031	0.039
10	100	1	1.5	0.010	0.009	30	40	1	2	0.022	0.018
10	100	1	2.5	0.010	0.009	30	40	1	2.5	0.028	0.018
10	100	2	1	0.045	0.043	30	40	2	1	0.106	0.100
10	100	2	2	0.041	0.043	30	40	2	1.5	0.076	0.078
10	100	2	2.5	0.040	0.043	30	40	2	2.5	0.077	0.078
20	4	0.5	2	0.091	0.099	30	100	0.5	1	0.014	0.030
20	4	0.5	2.5	0.080	0.099	30	100	0.5	2	0.009	0.009
20	4	1	1.5	0.133	0.123	30	100	0.5	2.5	0.010	0.009
20	4	1	2.5	0.087	0.099	30	100	1	1	0.017	0.030
20	4	2	2	0.355	0.347	30	100	1	1.5	0.012	0.009
20	4	2	2.5	0.374	0.347	30	100	1	2.5	0.017	0.009
20	10	0.5	1	0.098	0.083	30	100	2	1	0.062	0.064
20	10	0.5	1.5	0.047	0.063	30	100	2	2	0.044	0.043
20	10	0.5	2.5	0.035	0.044	30	100	2	2.5	0.045	0.043
20	10	1	1	0.094	0.083						

Table 13 Testing data sets of MARS predictions of ε_t

B (m)	Q	K_0	S_c	ε_{t_FDM} (%)	ε_{t_MARS} (%)	B (m)	Q	K_0	S_c	ε_{t_FDM} (%)	ε_{t_MARS} (%)
10	1	0.5	15	0.348	0.338	20	10	1	30	0.047	0.063
10	1	1	20	0.305	0.274	20	10	2	40	0.183	0.170
10	1	2	15	1.087	1.067	20	40	0.5	30	0.014	0.018
10	4	0.5	20	0.075	0.099	20	40	1	40	0.021	0.018
10	4	1	15	0.095	0.123	20	40	2	30	0.077	0.078
10	4	2	20	0.363	0.347	20	100	0.5	40	0.008	0.009
10	10	0.5	15	0.043	0.063	20	100	1	30	0.012	0.009

Table 13 Continued

B (m)	Q	K_0	S_c	ε_{t_FDM} (%)	ε_{t_MARS} (%)	B (m)	Q	K_0	S_c	ε_{t_FDM} (%)	ε_{t_MARS} (%)
10	10	1	20	0.049	0.044	20	100	2	40	0.043	0.043
10	10	2	15	0.185	0.190	30	4	0.5	60	0.113	0.099
10	40	0.5	20	0.014	0.018	30	4	2	75	0.310	0.347
10	40	1	15	0.020	0.018	30	10	0.5	45	0.047	0.063
10	40	2	20	0.078	0.078	30	10	1	60	0.051	0.044
10	100	0.5	15	0.008	0.009	30	10	2	45	0.173	0.190
10	100	1	20	0.010	0.009	30	40	0.5	60	0.015	0.018
10	100	2	15	0.043	0.043	30	40	1	45	0.021	0.018
20	4	0.5	30	0.168	0.123	30	40	2	60	0.075	0.078
20	4	1	40	0.088	0.099	30	100	0.5	45	0.009	0.009
20	4	2	30	0.358	0.371	30	100	1	60	0.013	0.009
20	10	0.5	40	0.034	0.044	30	100	2	45	0.043	0.043

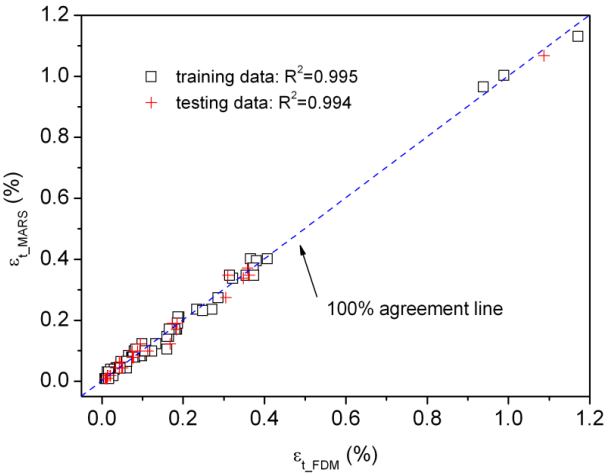

Fig. 7 Comparison between $\varepsilon_{t\ MARS}$ and $\varepsilon_{t\ FDM}$

For brevity, the ANOVA decomposition of the developed MARS model and the relative importance of the parameters are not detailed here. But the conclusion is that ε_t is mainly influenced by Q, followed by K_0. Table 14 lists the BFs of the MARS model for ε_t and their corresponding equations. The interpretable MARS model to predict ε_t is given by

$$\begin{aligned}&\varepsilon_{t\_MARS}(\%)\\&=0.1-0.0093\times BF1+0.046\times BF2+0.14\times BF3+0.074\times BF4\\&\quad-0.0004\times BF5+0.018\times BF6+0.025\times BF7+0.0007\times BF8\\&\quad+0.0013\times BF9+0.0084\times BF10+0.0018\times BF11+0.0043\times BF12\end{aligned} \tag{18}$$

Table 14 *BF*s and corresponding equations of MARS model for ε_t

*BF*s	Equation	*BF*s	Equation
*BF*1	max(0, Q - 4)	*BF*7	*BF*2×max(0, 2.5 - S_c/B)
*BF*2	max(0, 4 - Q)	*BF*8	max(0, Q - 40)
*BF*3	*BF*2 × max(0, K_0 -1)	*BF*9	max(0, 40 - Q) × max(0, 2 - S_c/B)
*BF*4	max(0, K_0 - 1)	*BF*10	max(0, Q - 10)
*BF*5	*BF*4 × max(0, Q -10)	*BF*11	max(0, 40 - Q) × max(0, K_0 - 1)
*BF*6	*BF*4 × max(0, 10 - Q)	*BF*12	max(0, 1.5 - S_c/B) × max(0, B - 20)

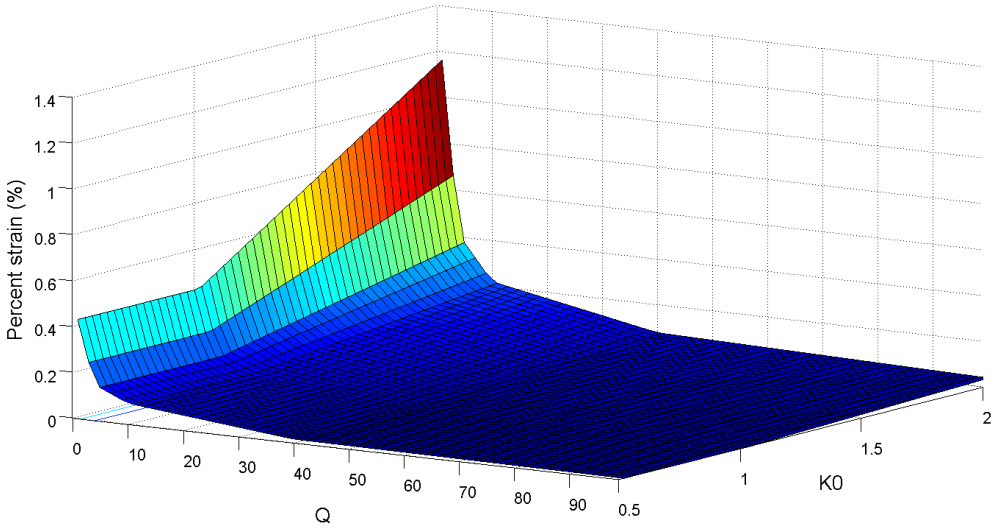

(a) Q and K_0

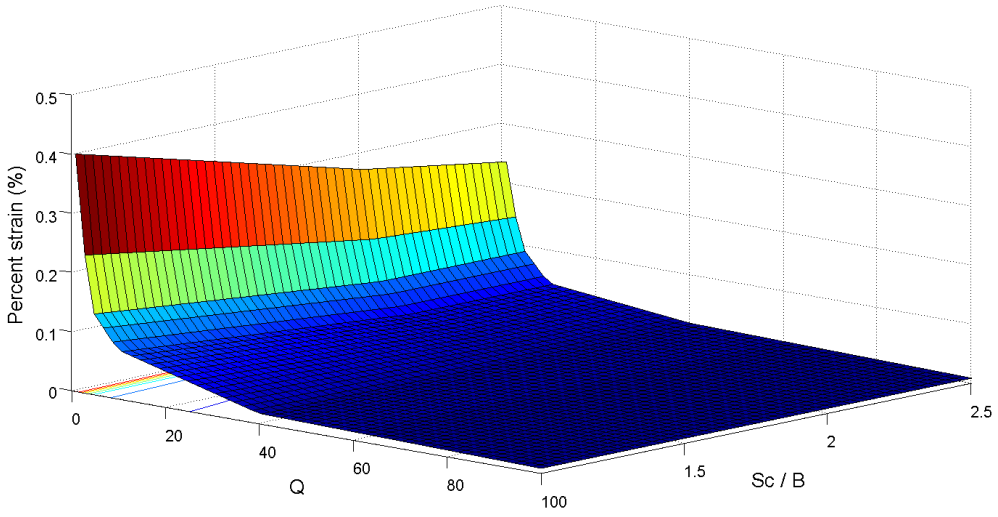

(b) Q and S_c/B

Fig. 8 Response surfaces relating ε_t to: (a) Q and K_0; (b) Q and S_c/B; and (c) Q and B

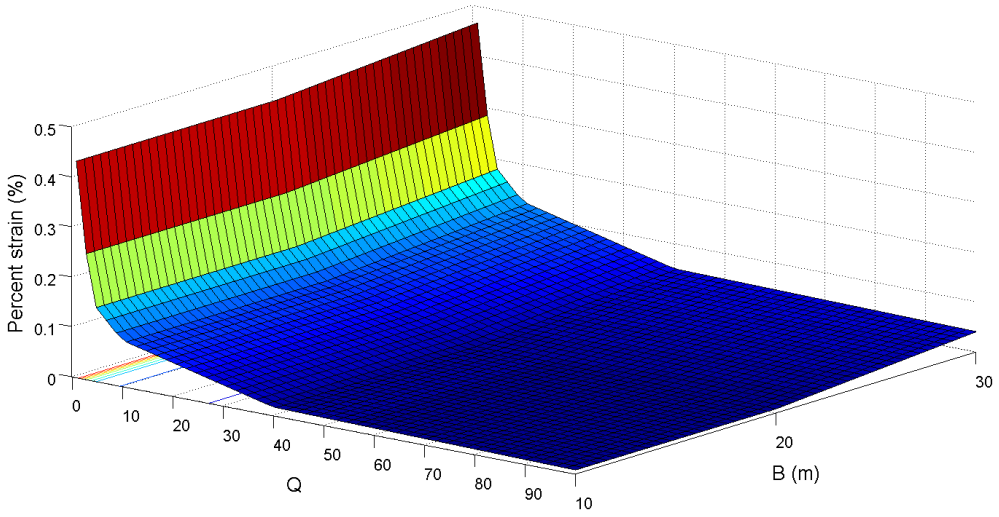

(c) Q and B

Fig. 8 Continued

The response surfaces relating ε_t to Q and K_0, Q and S_c/B, Q and B are illustrated in Fig. 8(a), (b) and (c), respectively. These response surfaces provide a practical design tool, especially during early design stages of design and construction. By specifying the pillar geometries S_c/B for a given Q as well as the cavern span, the expected percent strain can be estimated quickly. Or by assuming the threshold of the percent strain for a given Q and the cavern span, the appropriate pillar width can be estimated. Also, the effect of changing Q and in situ stress ratio K_0 can be assessed.

6. Probabilistic assessment on serviceability limit state

6.1 Serviceability criterion

The serviceability limit state can be assessed either by u_{max_t} or ε_t. However, there is very limited guidance from the literature with regard to the choice of a threshold displacement that can be utilized to limit the induced deformations with tolerable ranges. As a matter of fact, the choice of such a threshold value is specific to the size and shape of the openings and it does not provide information about the degree of stability. Consequently, Eq. (18), in terms of percent strain values ε_t, is adopted as the serviceability limit state criterion as explained in the following section.

6.2 Threshold strain values

Meguid and Rowe (2006) investigated the influence of rock mass strength reduction on the stability of D-shaped tunnels by examining the induced displacements at four different locations including the face centre, springline, crown and invert. They first obtained an elastic line which represents the elastic response of the rock mass. A design line, which is based on an additional 50% of the elastic strain ε_e, is then suggested to limit the induced strains to within tolerable limits.

Strains between the limits bounded by the elastic and design lines are considered to be acceptable and will not cause instability at those four locations.

Based on this design methodology, numerical trials are performed to derive the elastic responses under combinations of Q, K_0 and B. The elastic responses are obtained through FDM analyses with the rock mass assumed as linear elastic. Table 15 lists the elastic strains and the strain values for the design line. The strain value of the design line ε_d is 1.5 times that of the elastic strain ε_e.

Table 15 Elastic strains and the strain values of the design line

K_0	Q	B (m)	ε_e (%)	ε_d (%)
0.5	1	10	0.083	0.125
		20	0.084	0.126
		30	0.080	0.120
	4	10	0.050	0.075
		20	0.051	0.077
		30	0.050	0.075
	10	10	0.034	0.052
		20	0.035	0.053
		30	0.034	0.052
	40	10	0.020	0.030
		20	0.020	0.030
		30	0.020	0.030
	100	10	0.014	0.021
		20	0.014	0.021
		30	0.014	0.021
1	1	10	0.081	0.121
		20	0.082	0.123
		30	0.079	0.119
	4	10	0.045	0.068
		20	0.047	0.071
		30	0.046	0.070
	10	10	0.031	0.047
		20	0.033	0.049
		30	0.032	0.048
	40	10	0.018	0.027
		20	0.019	0.028
		30	0.018	0.027
	100	10	0.012	0.018
		20	0.013	0.019
		30	0.013	0.019

Table 15 Continued

K_0	Q	B (m)	ε_e (%)	ε_d (%)
2	1	10	0.147	0.221
		20	0.151	0.227
		30	0.154	0.231
	4	10	0.085	0.128
		20	0.087	0.131
		30	0.089	0.133
	10	10	0.059	0.088
		20	0.060	0.090
		30	0.061	0.092
	40	10	0.034	0.050
		20	0.034	0.052
		30	0.035	0.052
	100	10	0.023	0.035
		20	0.024	0.036
		30	0.024	0.036

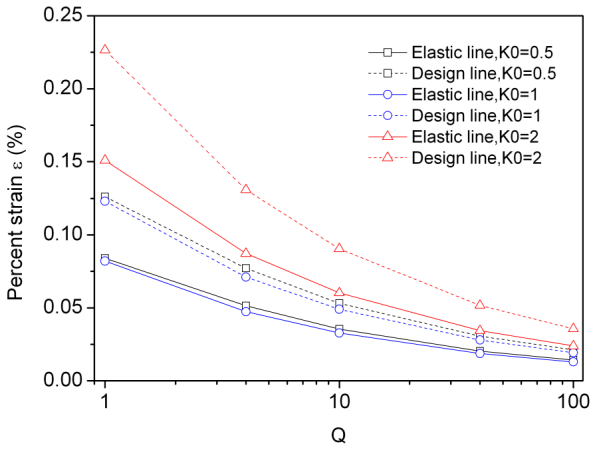

Fig. 9 Elastic and the design lines for K_0 = 0.5, 1 and 2

As the strain values for the three cases of B = 10, 20, and 30 m under the same K_0 and Q are nearly the same, it can be assumed that ε_d and ε_e are independent of the cavern span. Based on the strain values of Table 15, Fig. 9 plots the elastic line and the design line as a function of Q. It is clear that these lines are specific to K_0, as also indicated in Meguid and Rowe (2006).

Based on the results above, the design of underground rock cavern constructed in rock mass represented by Q under anisotropic/isotropic stress conditions represented by K_0 should satisfy the criterion of limiting the induced strain to within tolerable limits. The allowable strains ε_c are summarized in Table 16 for the cases of Q = 1, 4, 10, 40, and 100, respectively.

Table 16 Suggested ε_c for various Q values

Q	1	4	10	40	100
ε_c (%)	0.082-0.227	0.047-0.131	0.033-0.090	0.019-0.052	0.013-0.036

6.3 Reliability assessment using First-Order Reliability Method (FORM)

In many civil engineering applications, the assessment of safety is made by first establishing a relationship between the load S of the system and the resistance R. The boundary separating the safe and 'failure' domains is the limit state surface (boundary) defined by $G(x) = R - S = 0$, in which $\boldsymbol{x}$ = vector of random variables. Mathematically, $R > S$ or $G(x) > 0$ would denote a 'safe' domain. An unsatisfactory or 'failure' domain occurs when $R < S$ or $G(x) < 0$. Calculation of the probability of failure (probability of unsatisfactory performance) P_f involves the determination of the joint probability distribution of R and S and the integration of the Probability Density Function (PDF) over the failure domain. Considering that the PDFs of the random variables are not known in most rock engineering applications and the integration is computationally demanding when multi-variables are involved, an approximate method known as the First-Order Reliability Method (FORM) (Hasofer and Lind 1974), is commonly used to assess P_f. The approach involves the transformation of the limit state surface into a space of standard normal uncorrelated variables, wherein the shortest distance from the transformed limit state surface to the origin of the reduced variables is the reliability index β (Cornell, 1969). For normal distributed random variables, $P_f \approx 1 - \Phi(\beta)$, in which Φ = cumulative normal density function. Mathematically, Low and Tang (2004) have shown that β can be computed using

$$\beta = \min_{x \in F} \sqrt{\left[\frac{x_i - u_i}{\sigma_i}\right]^T [\boldsymbol{R}]^{-1} \left[\frac{x_i - u_i}{\sigma_i}\right]} \tag{19}$$

in which x_i is the set of n random variables, μ_i is the set of mean values, σ_i is the standard deviation, $\boldsymbol{R}$ is the correlation matrix and F is the failure region. Low (1996) has shown that Microsoft EXCEL spreadsheet can be used to perform the minimization and determine β.

In assessing the serviceability limit state (SLS) for twin caverns the limit state function based on the MARS model can be expressed as

$$\begin{aligned} g(\boldsymbol{x}) = g(\boldsymbol{x}) &= \varepsilon_c - \varepsilon_{t\_MARS} \\ &= \varepsilon_c - 0.1 - 0.0093 \times BF1 - 0.046 \times BF2 - 0.14 \times BF3 - 0.074 \times BF4 \\ &\quad + 0.0004 \times BF5 - 0.018 \times BF6 - 0.025 \times BF7 - 0.0007 \times BF8 \\ &\quad - 0.0013 \times BF9 - 0.0084 \times BF10 - 0.0018 \times BF11 - 0.0043 \times BF12 \end{aligned} \tag{20}$$

The expressions of BFs in this equation can be found in Table 14 and the statistics of the input variables assumed are shown in Table 17. It should be highlighted that the probability of failure P_f is significantly influenced by the choice of ε_c and usually when using the lower bound value of ε_c, the cavern performance is nearly elastic. Thus, in the following analyses, the upper bound values of ε_c are adopted based on the mean value of Q.

Table 17 Input variables for reliability assessment of SLS

Variable	Distribution type	Mean	*COV*
Q	Normal	10, 40, 100	0.1, 0.2, 0.3, 0.4
B	Normal	10, 20, 30	0.1
S_c/B	Normal	1, 1.5, 2, 2.5	0.1
K_0/B	Normal	0.5, 1, 2	0.1

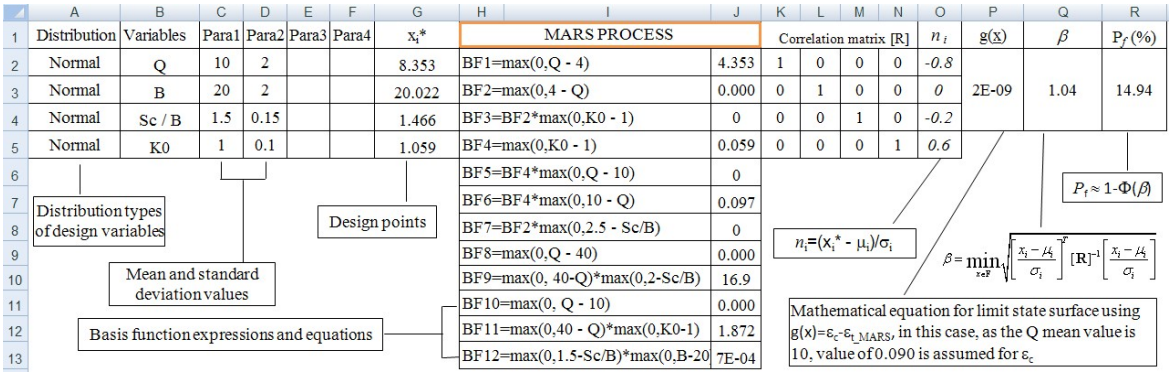

Fig. 10 Calculation of P_f for serviceability limit state using FORM_MARS spreadsheet

Probabilistic assessment of the percent strain ε_t can be performed using FORM based on the built MARS model. The serviceability limit state function Eq. (20) and its corresponding *BF* equations in Table 14 are incorporated into an EXCEL spreadsheet environment based on the approach by Low and Tang (2007), from which the reliability index can be determined. Fig. 10 shows a sample spreadsheet for computing the reliability index β where the statistics of the design parameters are the same as those used in the previous section. The spreadsheet cells A2:A5 allows the selection of various distribution types for the input variables, including normal, lognormal, triangular etc as explained in Low and Tang (2007). For nonnormals, the nonnormal distributions are replaced by an equivalent normal ellipsoid, centered at the equivalent normal mean. Cells C2:F5 are parameters which are set corresponding to the variable distribution types. For lognormals, cells C2:C5 correspond to the mean values while cells D2:D5 correspond to the standard deviations. The correlation matrix $\boldsymbol{R}$ in cells K2:N5 are used to define the correlations between Q, B, S_c/B and K_0. The n_i vector in cells O2:O5 contains equations for $(x_i - u_i^N)/\sigma_i^N$. Cells H2:J13 contain the basis function expressions and equations obtained from the MARS model. The design point (x^* values) was obtained by using the spreadsheet's built-in optimization routine SOLVER to minimize the cell, by changing the x^* values, under the constraint that the performance function $g(x^*) = 0$. Prior to invoking the SOLVER search algorithm, the x^* values were set equal to the mean values (10, 20, 1.5, 1) of the original random variables. Iterative numerical derivatives and directional search for the design point x^* were automatically carried out in the spreadsheet environment.

Fig. 11 plots the influence of the various design parameters on P_f of SLS. It is clear that both the *COV* and the average value of Q significantly influence the P_f. However, the influence of B on P_f is not as significant as that for S_c/B. In addition, from Fig. 11(c) it can be observed that the

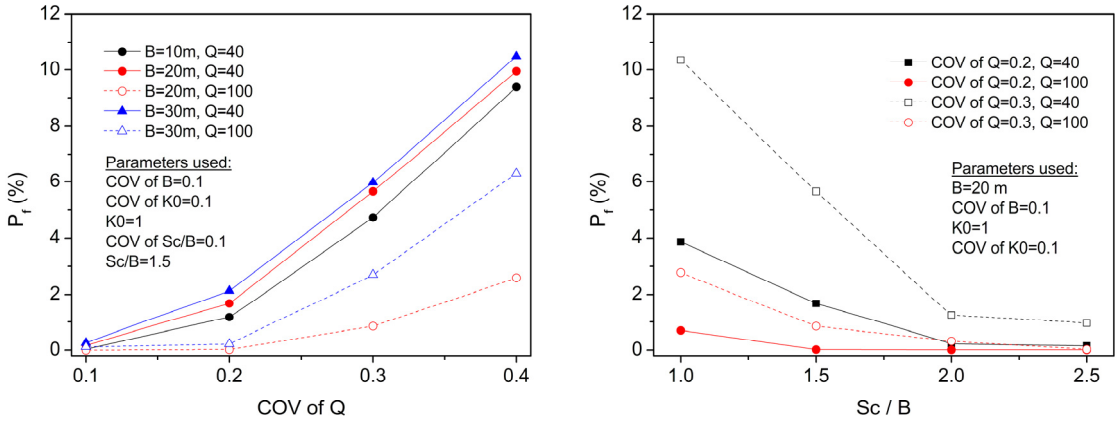

(a) *COV* of Q, B and mean Q (b) S_c/B, *COV* and mean Q

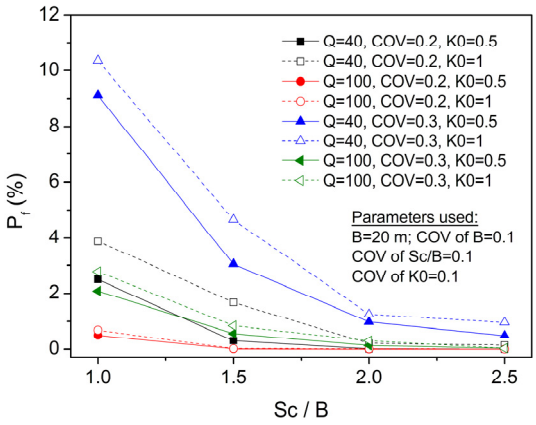

(c) S_c/B, K_0, *COV* and mean Q

Fig. 11 Influence of Q, S_c/B, B, and K_0 on P_f of SLS: (a) *COV* of Q, B and mean Q; (b) S_c/B, *COV* and mean Q; and (c) S_c/B, K_0, *COV* and mean Q

influence of K_0 on P_f is also significant when $Q = 40$ compared with $Q = 100$. The P_f under $K_0 = 1$ is generally higher than that under $K_0 = 0.5$ as the ε_t for $K_0 = 1$ is larger than for $K_0 = 0.5$ but ε_c is the same.

7. Conclusions

This paper considered the serviceability limit state of twin caverns. The dependent responses considered include the maximum key point displacement u_{max_t} and the percent strain ε_t. MARS model predicting the maximum key point displacement can be used to give preliminary estimates of the expected maximum cavern displacements during construction. The response surfaces relating percent strain ε_t to Q and K_0, Q and S_c/B, Q and B were constructed from the built MARS model.

Percent strain ε_t is adopted as the serviceability limit state criterion. The threshold strain values are determined through the elastic and design line methodology proposed by Meguid and Rowe (2006). Probabilistic assessments on SLS were performed using FORM spreadsheet method based on the built MARS percent strain model. This study will be extended to investigate the three-dimensional effects of the face advancement of a new cavern on the support of an adjacent existing cavern.

Acknowledgments

The authors would like to express their appreciation to the Defense Science and Technology Agency Singapore for providing the research funding for this research. The authors are most thankful to the two anonymous reviewers for their valuable comments and suggestions.

References

Aksoy, C.O., Ozacar, V. and Kantarci, O. (2010), "An example of estimating rock mass deformation around an underground opening using numerical modeling", *Int. J. Rock Mech. Min.*, **47**(2), 272-278.

Attoh-Okine, N.O., Cooger, K. and Mensah, S. (2009), "Multivariate adaptive regression spline (MARS) and hinged hyper planes (HHP) for doweled pavement performance modeling", *Constr. Build. Mater.*, **23**(9), 3020-3023.

Barton, N., Løset, F., Lien, R. and Lunde, J. (1980), "Application of Q system in design decisions concerning dimensions and appropriate support for underground installations", *Proceedings of the International Conference on Subsurface Space*, Rockstore, Stockholm, June, **Volume 2**, pp. 553-561.

Basarir, H. (2006), "Engineering geological studies and tunnel support design at Sulakyurt dam site, Turkey", *Eng. Geol.*, **86**(4), 225-237.

Bieniawski, Z.T. (1978), "Determining rock mass deformability: experience from case histories", *Int. J. Rock Mech. Min. Sci. Geomech. Abstr.*, **15**(5), 237-247.

Bieniawski, Z.T. (1989), *Engineering Rock Mass Classifications*, John Wiley and Sons, New York, USA.

Cornell, C.A. (1969), "A probability-based structural code", *ACI*, **66**(12), 974-985.

Friedman, J.H. (1991), "Multivariate adaptive regression splines", *Ann. Stat.*, **19**(1), 1-141.

Gandomi, A.H. and Roke, D.A. (2013), "Intelligent formulation of structural engineering systems", *7th M.I.T. Conference on Computational Fluid and Solid Mechanics-Focus: Multiphysics & Multiscale*, Massachusetts Institute of Technology, Cambridge, MA, USA, June.

Goh, A.T.C., Xuan, F. and Zhang, W.G. (2013), "Reliability assessment of diaphragm wall deflections in soft clays", *Foundation Engineering in the Face of Uncertainty* (*GSP 229*) *ASCE*, 487-496.

Goh, A.T.C. and Zhang, W.G. (2012), "Reliability assessment of stability of underground rock caverns", *Int. J. Rock Mech. Min.*, **55**, 157-163.

Goh, A.T.C. and Zhang, W.G. (2014), "An improvement to MLR model for predicting liquefaction-induced lateral spread using multivariate adaptive regression splines", *Eng. Geol.*, **170**, 1-10.

Hasofer, A.M. and Lind, N. (1974), "An exact & invariant first-order reliability format", *J. Eng. Mech. ASCE*, **100**(1), 111-121.

Hastie, T., Tibshirani, R. and Friedman, J. (2009), *The Elements of Statistical Learning: Data Mining, Inference and Prediction*, (2nd Ed.), Springer.

Hoek, E. and Brown, E.T. (1997), "Practical estimates of rock mass strength", *J. Rock Mech. Min.*, **34**(8), 1165-1186.

Itasca Consulting Group (2005), *FLAC-3D, User's Guide: Fast-Lagrangian Analysis of Continua in 3 Dimensions-Version 3.0*, Minneapolis, MN, USA.

Jekabsons, G. (2010), *VariReg*: *A Software Tool for Regression Modeling using Various Modeling Methods*, Riga Technical University, Latvia, URL: http://www.cs.rtu.lv/jekabsons/.
Lashkari, A. (2012), "Prediction of the shaft resistance of non-displacement piles in sand", *Int. J. Numer. Anal. Met.*, **38**(7), 904-931.
Low, B.K. (1996), "Practical probabilistic approach using spreadsheet", *Uncertainty in the Geologic Environment* (*GSP 58*) *ASCE*, Reston, VA, USA, pp. 1284-1302.
Low, B.K. and Tang, W.H. (2004), "Reliability analysis using object-oriented constrained optimization", *Struct. Saf.*, **26**(1), 69-89.
Low, B.K. and Tang, W.H. (2007), "Efficient spreadsheet algorithm for first-order reliability method", *J. Eng. Mech. ASCE*, **133**(12), 1378-1387.
Meguid, M.A. and Rowe, R.K. (2006), "Stability and D-shaped tunnels in a Mohr-Coulomb material under anisotropic stress conditions", *Can. Geotech. J.*, **43**(3), 273-281.
Mirzahosseinia, M., Aghaeifarb, A., Alavic, A., Gandomic, A. and Seyednour, R. (2011), "Permanent deformation analysis of asphalt mixtures using soft computing techniques", *Expert Syst. Appl.*, **38**(5), 6081-6100.
Palmstrom, A. (2000), "On classification systems", *Proceedings GeoEng2000*, Melbourne, Vic, Australia, November.
Samui, P. (2011), "Determination of ultimate capacity of driven piles in cohesionless soil: a multivariate adaptive regression spline approach", *Int. J. Numer. Anal. Met.*, **36**(11), 1434-1439.
Samui, P. and Karup, P. (2011), "Multivariate adaptive regression spline and least square support vector machine for prediction of undrained shear strength of clay", *IJAMC*, **3**(2), 33-42.
Serafim, J.L. and Pereira, J.P. (1983), "Considerations of the geomechanics classification of Bieniawski", *Proceedings of the International Symposium on Engineering Geology and Underground Construction*, Lisbon, Portugal, **Volume 1**, pp. 1133-1142.
Tugrul, A. (1998), "The application of rock mass classification systems to underground excavation in weak lime stone, Ataturk dam", *Turk. Eng. Geol.*, **50**(3-4), 337-345.
Zarnani, S., El-Emam, M. and Bathurst, R.J. (2011), "Comparison of numerical and analytical solutions for reinforced soil wall shaking table tests", *Geomech. Eng., Int. J.*, **3**(4), 291-321.
Zhang, W.G. and Goh, A.T.C. (2012), "Reliability assessment on ultimate and serviceability limit states and determination of critical factor of safety for underground rock caverns", *Tunn. Undergr. Sp. Tech.*, **32**, 221-230.
Zhang, W.G. and Goh, A.T.C. (2013), "Multivariate adaptive regression splines for analysis of geotechnical engineering systems", *Comput. Geotech.*, **48**, 82-95.

CC